Physics of Plasmas ARTICLE pubs.aip.org/aip/pop

Theory of CARM devices: The free electron laser perspective

Cite as: Phys. Plasmas **32**, 123105 (2025); doi: 10.1063/5.0283775
Submitted: 1 July 2025 · Accepted: 25 November 2025 ·
Published Online: 17 December 2025

Emanuele Di Palma[a] and G. Dattoli[b]

AFFILIATIONS

C. R. Enea Frascati, Nuclear Department, Via E. Fermi, 45-00045 Frascati, Rome, Italy

[a]Author to whom correspondence should be addressed: emanuele.dipalma@enea.it
[b]Electronic mail: pinodattoli@libero.it

ABSTRACT

The cyclotron autoresonance maser (CARM) has been developed since the seventies of the last century. It grew in parallel with the undulator-based free electron laser theoretical and experimental efforts. Authoritative studies have pointed out the relevant analogies and distinctive features of these devices. The intrinsic efficiency, significantly larger for the first, is one of its characterizing features, which has generated considerable interest in its application as an external source for additional plasma heating in fusion research. The development of CARM theory has revealed how the electron beam qualities constitute a bottleneck, severely limiting overall performance. In this direction, significant efforts have focused on designing these devices and developing practical tools for their design. This article describes the development of a theoretical framework of the CARM theory, providing essential elements to guide the design of these devices.

I. INTRODUCTION

Both cyclotron autoresonance maser (CARM) and free electron laser (FEL) are sources of coherent radiation based on beams of free electrons. They are laser-like means, whose active medium is not provided by bound electrons, as in atomic or molecular environments.[1–6] Although the formulation of the relevant theory started about six decades ago, they are the result of a longer scientific story, tracing back to the thirties of the last century with the development of the Klystron,[7,8] which later led to progress in traveling wave tubes (TWTs)[9,10] and gyrotrons.[11–15] For the state of the art of this technology, particularly with reference to high-power devices, see Ref. 16.

The common element of these devices is the transformation of the electron kinetic energy into electromagnetic radiation.[17] In other words, a fraction of the electron beam power is transformed into radiation power at a definite wavelength. The "fraction" we have mentioned is a quantity of paramount importance, known as the efficiency of the device.

The steps leading to the process of power "extraction" from one to the other beam include

(a) a mechanism allowing a frequency selection,
(b) a device allowing the coupling between the electron beam and the radiation field,
(c) a gain process and the associated mechanisms leading to saturation.

In the case of an undulator-based FEL, steps (a)–(c), realized by means of a magnet with spatial oscillations (peak field B_0), are easily recognized. The tools utilized in such a process are a beam of relativistic electrons injected into an undulator magnet, with a transverse static spatially oscillating such that

$$B \propto B_0 e^{ik_u z}, \quad k_u = \frac{2\pi}{\lambda_u}, \tag{1}$$

where λ_u is the spatial period.

The electrons moving inside the undulator emit bremsstrahlung radiation. From an elementary point of view, the process can be viewed as a Compton backscattering of pseudo-photons, characterized by the frequency $\omega_u = k_u c$,[18] which are up-shifted to

$$\omega = \omega_u + k v_z \to \omega = \frac{\omega_u}{1-\beta_z}, \quad \beta_z = \frac{v_z}{c}. \tag{2}$$

This constitutes the frequency selection mechanism [see steps (a), (b), and (c)]. Steps (b) and (c) are summarized below.

The Lorentz force induces a transverse velocity $v_\perp$ and a consequent variation of the longitudinal velocity v_z according to

$$\beta_\perp = \frac{K_u}{\sqrt{2}\gamma}c,$$
$$K_u = \frac{eB_0\lambda_u}{2\pi mc} \equiv \text{undulator strength parameter}, \tag{3}$$
$$\beta_z = \sqrt{1-\frac{1}{\gamma^2}\left(1+\frac{K_u^2}{2}\right)} \cong 1-\frac{1}{2\gamma^2}\left(1+\frac{K_u^2}{2}\right),$$

the last equality on the right holds for the relativistic factor $\gamma \gg 1$, as in the majority of U-FEL.

The longitudinal velocity, once plugged in Eq. (2), yields the explicit expression of the FEL operating frequency, in terms of the electron energy and undulator parameters. The transverse velocity is the key element, allowing coupling to an electromagnetic field co-propagating with the electron along the z-axis. The successive evolution of the process is characterized by beam energy modulation, bunching, coherent emission as well as saturation. These are the same mechanisms (albeit achieved by other means) characterizing the physics of TWT.

The CARM operating principle can be described along the same lines. It exploits a moderately relativistic e-beam injected into the waveguide of a resonant cavity, where an axial static magnetic field constrains the electrons (see Fig. 1) along a helical path characterized by the cyclotron frequency given by

$$\Omega_{c0} = \frac{eB_0}{m_e}, \tag{4}$$
$$m_e \equiv \text{electron mass},$$

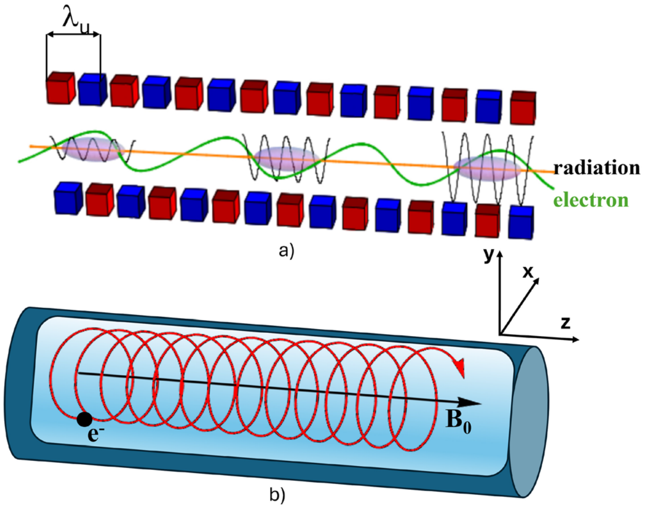

FIG. 1. (a) The electrons, initially moving along the undulator axis (z-direction), are affected by the Lorentz force and execute a "wiggling" trajectory (the green trajectory presented in the figure is just an exemplification of the electron motion which is subject to the Lorentz force oscillating in the x-z plane, because the field is supposed to be polarized along the y-axis). The interaction with the wave induces energy modulation in the electron beam followed by bunching at the field wavelength, eventually leading to the coherent emission process. (b) The electrons, with longitudinal and transverse velocities, move inside a solenoidal magnetic field B_0, execute helical trajectories, and interact with a co-propagating mode cavity, eventually inducing the coherent emission process.

and period

$$\Lambda = 2\pi\frac{c}{\Omega}, \quad \Omega = \frac{\Omega_{c0}}{\gamma}. \tag{5}$$

The electrons are likely to lose power by "pumping" a selected cavity mode, provided that the appropriate resonance conditions are satisfied.

The previous description is essentially a rewording of what we said for the undulator FELs. The significant difference stems because the interaction process occurs in a waveguide (WG) and therefore the relevant description should include the constraints imposed by the WG.

It should be accordingly emphasized that the electromagnetic wave propagates along the z direction, with a wave vector linked to the phase velocity (v_ϕ) by the identity

$$k_z = \frac{\omega}{v_\phi}. \tag{6}$$

The kinematics of the electron motion is summarized by the equations

$$\beta_z^2 + \beta_\perp^2 = 1-\gamma^{-2},$$
$$\beta_{z,\perp} = \frac{v_{z,\perp}}{c}, \quad \alpha = \frac{v_\perp}{v_z}. \tag{7}$$

We can establish the following analogies between CARM and FEL devices:

$$\Lambda \leftrightarrow \lambda_u, \quad K_u \leftrightarrow \frac{\beta_\perp}{\gamma}. \tag{8}$$

The first correspondence naturally emerges from Fig. 1, after noting that the electron path is similar to that of electrons in a helical undulator, the second is derived from the first of Eq. (3) according to which the electron induced transverse model is directly linked to the undulator strength parameter.

The resonance condition is an extension of Eq. (2),

$$\omega = \frac{\Omega_{c0}}{\gamma} + k_z c\beta_z, \tag{9}$$

which, once coupled with the cavity dispersion condition given by

$$\omega^2 = c^2(k_\perp^2 + k_z^2), \tag{10}$$

yields the frequency selection intersections shown in Fig. 2 and presented below,

$$\omega_\pm = \Omega\frac{1\pm\beta_z\sqrt{1-(1-\beta_z^2)\left(\frac{\omega_c}{\Omega}\right)^2}}{1-\beta_z^2}, \quad \omega_c = ck_\perp. \tag{11}$$

If the condition $\left((1-\beta_z^2)\left(\frac{\omega_c}{\Omega}\right)^2\right) \ll 1$ holds, we have

$$\omega_\pm \approx \Omega\frac{1\pm\beta_z\left[1-\frac{1}{2}(1-\beta_z^2)\left(\frac{\omega_c}{\Omega}\right)^2\right]}{1-\beta_z^2}. \tag{12}$$

Furthermore, assuming the last term in square brackets is completely negligible, we eventually obtain the up-shifted (double Lorentz shift, CARM mode) frequency ω_+ and lower frequency ω_-,

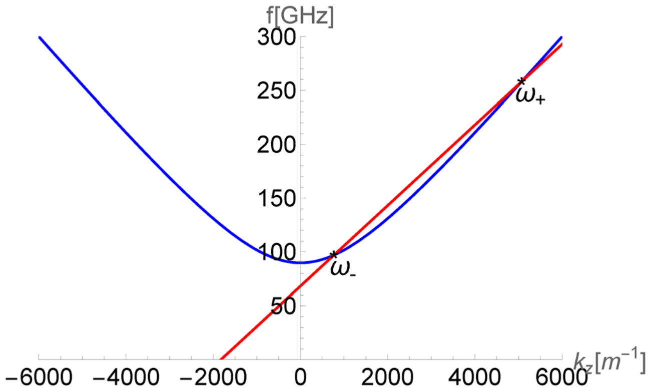

FIG. 2. CARM Brillouin diagram: Cavity dispersion curve (blue), electron line (red). The intersection points (ω_+, ω_-) fix the operating frequencies (CARM and gyrotron, respectively).

$$\begin{aligned} \omega_+ &\approx \frac{\Omega}{1-\beta_z}, \\ \omega_- &\approx \frac{\Omega}{1+\beta_z}. \end{aligned} \tag{13}$$

The approximation, valid for relativistic particles, yields $\omega^+ \approx 2\gamma^2\Omega$. In the following, we take the full expression for the forthcoming analytical and numerical computation because the relativistic assumption is not strictly verified.

The physical content of Eqs. (13) is of paramount importance. Two frequencies are selected, and this is a first indication that, along with noticeable analogies, CARM and U-FEL have important distinctive features, which are carefully discussed in this article.

In the forthcoming sections of the article, we discuss various aspects of the CARM dynamics. In Sec. II, we analyze the linear regime, derive the gain equation in low and high gain regimes. The linear and saturated dynamics are discussed in Sec. III using the 1D home-made code GRAAL (Gyrotron Radiation Amplification Autoresonance Laser). We focus on the saturation mechanisms, which are displayed on the Brillouin diagram. The operation at lower frequency, briefly touched on in Sec. IV, exhibits peculiar differences compared to the up-shifted mode, which requires an *ad hoc* treatment, and is postponed to a forthcoming investigation.

II. CARM LINEAR REGIME

The preliminary discussion of CARM physics given in Sec. I provides guidance for formulating a set of equations capable of describing the relevant dynamics.

The theoretical description has been developed in important research,[5,19] clarifying the underlying physics and providing tools for elaborating numerical codes,[20,22] yielding a quantitative account of the experimental results[23–25] and establishing design criteria of CARM amplifiers.[26,27]

Before proceeding further, we emphasize again that, unlike undulator-based devices, the CARM exhibits two resonance frequencies, which can be excited by the use of an initial seed and by properly adjusting the electron beam for the up- or down-shifted frequency.

We have presented in Eqs. (14) and (15) the set of equations representative of the one-dimensional evolution for an ensemble of electrons, governed by an axial magnetic field, interacting with waveguide electromagnetic modes.[28] The structure of the equations is equivalent to those modeling the U-FEL dynamics, presented, e.g., in Ref. 29. They consist of two blocks. The first three are relevant to the evolution of electron kinetic variables, energy γ, normalized transverse and longitudinal velocities $\beta_\perp$, β_z (the index i denotes the ith particle out of a total N_p). In Eqs. (14), θ denotes the electron phase variable and δ is the wave phase shift, developing during the interaction (for further details, see Refs. 19, 20, 22, and 28). The pivotal role of this term in CARM dynamics is discussed in Sec. IV.

The evolution of the normalized field amplitude a_+, ruling the strength of the interaction, is provided by Eq. (15), which include the average taken on the electrons' dynamical variables

$$\begin{aligned} \frac{d\gamma_i}{dz} &= -a_+ k \frac{\beta_{\perp i}}{\beta_{z,i}} \sin(\theta_i), \\ \frac{d\theta_i}{dz} &= \frac{\Omega_{c0}}{\gamma_i c \beta_{z,i}} - \frac{k}{\beta_{zi}}\left(1-\frac{\beta_{z,i}}{\beta_\phi}\right) - \frac{a_+ k}{\gamma_i \beta_{\perp i}\beta_{z,i}} \\ &\quad \times \left(1-\frac{\beta_{z,i}}{\beta_\phi}\right)\cos(\theta_i) - \frac{d\delta}{dz}, \\ \frac{d\beta_{\perp i}}{dz} &= \frac{a_+ k}{\gamma_i \beta_{z,i}}\left(\beta_{\perp i}^2 - 1 + \frac{\beta_{z,i}}{\beta_\phi}\right)\sin(\theta_i), \end{aligned} \tag{14}$$

and

$$\begin{aligned} \frac{da_+}{dz} &= \frac{\mu_0 e}{m_e c}\frac{J_{0,eff}}{2k_z}\frac{1}{N_p}\sum_{i=1}^{N_p}\frac{\beta_{\perp i}}{\beta_{z,i}}\sin(\theta_i), \\ \frac{d\delta}{dz} &= -\frac{\mu_0 e}{m_e c}\frac{J_{0,eff}}{2k_z a_+}\frac{1}{N_p}\sum_{i=1}^{N_p}\frac{\beta_{\perp i}}{\beta_{z,i}}\cos(\theta_i), \end{aligned} \tag{15}$$

being $J_{0,eff}$ the beam current density overlapping the operative mode in the cavity (for more details, see Appendix A).

The numerical integration of the above set of equations is an important step, if one is interested in the dynamics including the saturated regime, dominated by strong nonlinear effects (see Appendix C for the code operating conditions).

However, important information can be obtained in the weak coupling regime, which is tractable analytically.

The derivation of the linear regime equations follows the scheme outlined below and detailed in Appendix B.

We follow the method developed in Ref. 30 and first note that Eqs. (14) and (15) can be handled to derive a pendulum-like equation given by

$$\begin{aligned} \frac{d^2\alpha}{dz^2} &\cong H_0 a_+ \sin(\theta), \\ \alpha &= \theta + \delta, \end{aligned} \tag{16}$$

where we define H_0 according to Appendix B, with dimensions of the inverse of a surface,

$$H_0 = fk^2, \tag{17}$$

and f is a function of the beam kinematic quantities and of the waveguide propagation conditions (see Appendix B).

Next, the use of the “interaction” amplitude given by

$$A = a_+ e^{i\delta} \tag{18}$$

allows to cast Eq. (16) in the form

$$\frac{d^2\alpha}{dz^2} = H_0 a_+ \sin(\alpha - \delta) = -H_0\, Im(Ae^{-i\alpha}). \tag{19}$$

The small signal approximation is obtained by perturbing the argument of the exponential on the rhs of Eq. (19), namely,

$$\alpha \approx \alpha_0 + \nu_0 z + \Delta\alpha, \tag{20}$$

where α_0, ν_0 are the initial conditions of the differential equation (19) with $\Delta\alpha \ll 1$.

Plugging this[20] into Eq. (19) and neglecting $\Delta\alpha$ in the argument of the exponential, we find

$$\Delta\alpha \approx -H_0 \int_0^z dz'(z - z')Im\Big(A(z')e^{-i(\alpha+\nu_0 z')}\Big), \tag{21}$$

and it is also easily recognized that

$$\nu_0 = \frac{d\alpha}{dz}\bigg|_{z=0} = \frac{k}{\beta_{z0}}\frac{\omega - \omega_+}{\omega_+} = \frac{k}{\beta_{z0}}\Delta_0, \tag{22}$$

assuming the average of $\cos(\theta_i)$ over the particles at $z = 0$ to be zero and varying Ω_{c0} for Δ_0 (the CARM detuning has been defined with a minus sign with respect to the U-FEL counterpart).

The use of the “average bracket” notation,

$$\langle \ldots \rangle_{\theta_0} \to \frac{1}{N_p}\sum_i (\ldots.)_i, \tag{23}$$

allows to write Eqs. (15) as

$$\begin{aligned} \frac{da_+}{dz} &= K\left\langle \frac{\beta_\perp}{\beta_z}\sin(\theta)\right\rangle_{\theta_0}, \\ \frac{d\delta}{dz} &= -\frac{K}{a_+}\left\langle \frac{\beta_\perp}{\beta_z}\cos(\theta)\right\rangle_{\theta_0}. \end{aligned} \tag{24}$$

A comment on the meaning and evaluation of the averaging procedure is necessary. We emphasize that it consists of two different averages: on the electron phase distribution and on the energy velocities distributions which are assumed to be uncorrelated.[31]

The coupling parameter K is defined as

$$K = \frac{\mu_0 e}{m_e c}\frac{J_{0,eff}}{2k_z}. \tag{25}$$

It should be noted that K has physical dimensions of the inverse of a length and can be written in alternative form as

$$K = \frac{2\pi}{k_z}\frac{J_{0,eff}}{I_A}. \tag{26}$$

The derivative of A with respect to z reads

$$\frac{dA}{dz} = -iK\left\langle \frac{\beta_\perp}{\beta_z}e^{i\alpha}\right\rangle_{\alpha_0}, \tag{27}$$

and, using the approximations,[19,20] we eventually find for A the following integral equation, representing its small signal approximation:

$$\frac{dA}{dz} = -iK\left\langle \frac{\beta_\perp}{\beta_z}e^{i\alpha_0}\right\rangle_{\alpha_0} e^{i\nu_0 z} + \frac{i}{2}KH_0 b_2 \int_0^z dz'(z - z')A(z')e^{i\nu_0(z-z')}. \tag{28}$$

The first term is associated with an initially bunched electron beam[30] and will be overlooked in the first instance. The importance of its role will be discussed later in this section.

Using standard techniques (see Ref. 30 and Appendix B), Eq. (28) can be reduced to the third order differential equations given by

$$\begin{gathered} A''' - 2i\nu_0 A'' - \nu_0^2 A' = \frac{i}{2}\Gamma A, \quad \Gamma = KH_0 b_2, \quad (') = d/dz, \\ A(0) = a_+, \quad A'(0) = 0, \quad A''(0) = 0, \\ b_2 = \left\langle \frac{\beta_\perp}{\beta_z}\right\rangle_{\alpha_0}. \end{gathered} \tag{29}$$

It is worth noting that the term b_2, which is directly linked to the transverse velocity, plays the role of an effective coupling between the electrons and the field and can be included in the definition in the coefficient Γ. The bracket considers the average on velocity distributions, in the case of a non-ideal electron beam. The choice of the initial conditions reflects the operating regime of the starting coherent emission process, those of Eqs. (29) are relevant to the case of a seeded amplification.

Both Eqs. (28) and (29) have been written in a form equivalent to those discussed for U-FEL and have been widely exploited in the literature concerning TWT and FEL (in their wider meaning, even before they were proposed for the study of high gain U-FEL devices).[32,33]

A particularly useful form of solution is provided by the Fang–Torre formula (see Appendix B), derived in an unpublished note and detailed in a recent article,[34] which the reader can check for comparison.

In Fig. 3, we gain is defined as

$$G(\Delta_0) = \frac{|A(z)|^2 - |A(z = 0)|^2}{|A(z = 0)|^2} \tag{30}$$

and evaluated at specific positions on the z-axis and plotted vs the detuning parameter $\Delta_0 = \nu_0\beta_{z0}/k$.

In Fig. 3, the small signal curve (dotted) has been superimposed to the numerical solution to check the consistency of the approximation procedure. In Sec. III, we will discuss more thoroughly the strong signal regime dynamics, for the moment we emphasize that the agreement between numerical and analytical results is reasonable. The upper part of the figure reports the gain curve, evaluated at different positions on the power growth curve. The transition from low to high gain regimes is evident, as also reported in Ref. 34, where the same pattern has been emphasized for the U-FEL dynamics (note that the discrepancy of the position of the maximum gain peak is due to difference in sign of the definition of the respective detunings). As we consider the linear regime only, we have limited the comparison to few points on the power curve. For larger power values, significant deviations occur due to nonlinear effects extraneous to the small signal regime.

In Fig. 3 we have reported the CARM gain vs. the detuning. The operating parameters have been chosen to ensure “low gain” conditions. We like to underscore that spectral content is closely similar to that exibited by the U-FEL devices with tapered undulators, as commented in Sec. III it resembles that of FEL operating with tapered undulators.[35]

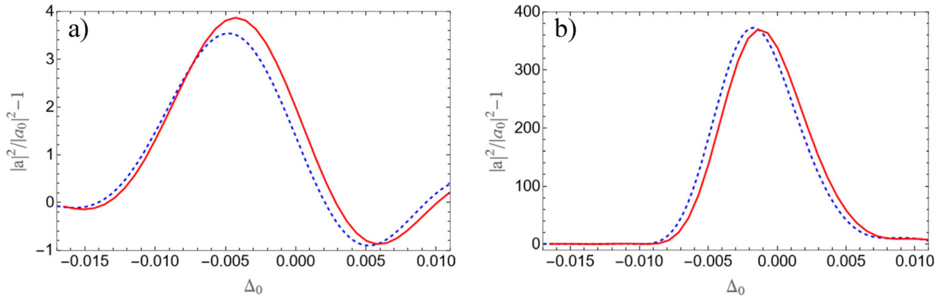

FIG. 3. Comparison between numerical (solid line) and analytical (dot line) computations of the CARM small signal gain, at different points on the z-axis: (a) $z = 0.14$, (b) $z = 0.315$ m. The numerical simulations have been performed using the parameters presented in Table I.

The comments regarding the evolution of the CARM power reflect the dynamics of the FEL-like coherent light sources. After a lethargy region, during which bunching develops, the power is characterized by an exponential growth governed by the fastest growing root of the third-degree algebraic equation associated with Eq. (29). Considering for simplicity $\nu_0 = 0$, we can write the solution as

$$A(z) \approx \sum_{j=0}^{2} c_j e^{\lambda_j z}, \quad \lambda_j = \frac{r_j}{\sqrt[3]{2}\Gamma^{1/3}}, \tag{31}$$

where r_j are the cubic roots of the imaginary unit and c_j depend on the initial conditions. The slope of the power growth depends on the real positive part of λ_j.

Before proceeding further, we provide a more practical form of the CARM growth rate. We therefore note that if we select the "+" root in Eq. (13), we find

$$\left(\frac{\Gamma}{2}\right)^{1/3} = \frac{1}{\sqrt[3]{2}}\left(\frac{2\pi f b_2 k^2}{k_z}\frac{J_{0,eff}}{I_A}\right)^{1/3}. \tag{32}$$

The physical dimensions of the previous cubic root and the exponential in Eq. (31) can be written as

$$e^{\lambda_j z} = e^{r_j z/L_{gc}}, \quad L_{gc} = \sqrt[3]{2}\left(\frac{2\pi \mathrm{f b_2 k^2}}{\mathrm{k_z}}\frac{\mathrm{J}_{0,eff}}{\mathrm{I_A}}\right)^{-1/3}, \tag{33}$$

where L_g has the same role of the gain length as in undulator FELs.

Finally, following the procedure outlined in Appendix B, we find

$$|A(z)|^2 \approx \frac{1}{9}A_0^2\left[3 + 2\cosh\left(\sqrt{3}\bar{z}\right) + 4\cos\left(\frac{3}{2}\bar{z}\right)\cosh\left(\frac{\sqrt{3}}{2}\bar{z}\right)\right], \quad \bar{z} = \frac{z}{L_{gc}}, \tag{34}$$

which, even though simplified, reproduces the essential features of the small signal power growth vs z (see Fig. 4).

We have presented in Fig. 3 the gain vs the detuning parameter, at different positions on the propagation direction. We have also noted a kind of transition from the low to the high gain regime, characterized by a modification of the gain curve shape.

We adopt a more direct argument, based on a perturbative treatment of the Volterra integrodifferential equation given by

$$\frac{dA}{dz} = \frac{i}{2}KH_0 b_2 \int_0^z dz'(z - z')A(z')e^{i\nu_0(z-z')}, \tag{35}$$

admitting solutions based on the iterative procedure presented below (for the perturbative treatment of Volterra equations, see Ref. 36),

$$A \approx \sum_{n=0}^{N} \epsilon^n \tilde{A}_n, \quad \epsilon = \frac{i}{2}b_2 K H_0,$$
$$\frac{d\tilde{A}_n}{dz} = \int_0^z dz'(z - z')\tilde{A}_{n-1}(z')e^{i\nu_0(z-z')}, \tag{36}$$
$$A_n(0) = a(0)\delta_{n,0}, \quad n \geq 0.$$

Each level of the approximation can be used to derive the corresponding gain curve, as noted below. The gain curves, at different levels of approximation, are shown in Fig. 5.

In this section, we have discussed several aspects of CARM dynamics in the linear regime, maintaining a description as close as possible to the treatment of U-FEL devices. In Sec. III, we extend the analysis to the strong signal regime, where key differences become apparent.

III. CARM STRONG SIGNAL REGIME AND SATURATION

Before addressing the main topic of this section, it is worth commenting on an aspect of the small signal regime, we have just mentioned in Sec. II: the effect of electron-beam pre-bunching on the CARM power evolution dynamics. We have noted that this regime can be characterized in simple terms, by adding to the high gain integral equation a homogeneous contribution, depending on the initial phase distribution. For a non-uniformly phase distributed beam, the homogeneous term appearing in Eq. (28) and defined by an average

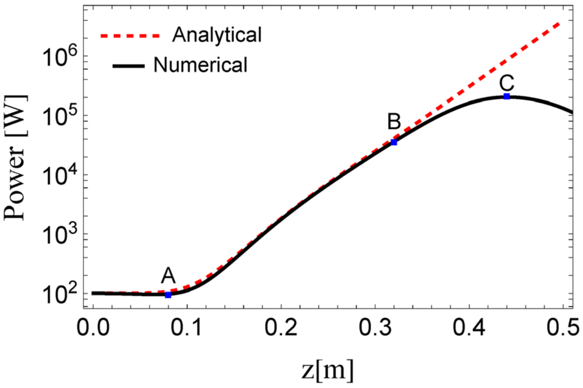

FIG. 4. Comparison between analytical [Eq. (34) dotted line] power growth and numerical solution (continuous line) including nonlinear regime. Bullets A, B, C denote the end of the lethargy region, onset of the nonlinear regime as well as the maximum saturated power, respectively.

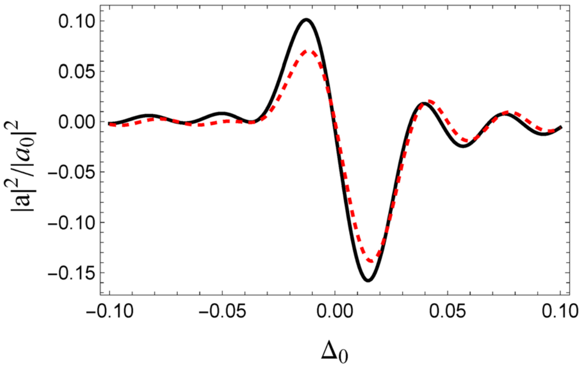

FIG. 5. Comparison between gain curves from numerical (continuous line) and perturbative solutions (dashed line) at $z = 0.049$. Note that the sign convention of CARM detuning is opposite to the FEL case.

on the initial phases α_0 is no more vanishing and is introduced in the computation as a bunching coefficient such that

$$b_u = \left\langle \frac{\beta_\perp}{\beta_z} e^{i\alpha} \right\rangle_{\alpha_0}, \tag{37}$$

it apparently vanishes when the integral equation is transformed into the third-order differential equation, which remains the same as Eq. (29) but with modified initial conditions. Physically, this means that the CARM signal may grow if the beam is bunched, even with a vanishing initial seed.

An example of CARM power growth from a bunched electron beam is shown in Fig. 6(a), where we have compared small-signal analytical solution and numerical computation (dotted-dashed and continuous lines, respectively).

In Fig. 6(b), we have compared the seedless operation (numerical) with the seeded operation (analytical linear regime).

The physical interpretation of Fig. 6 is that initial bunching dominates the early stages of growth, and exponential growth is seen when self-induced bunching surpasses the contribution from the initial non-uniform phase distribution. It is important to underscore that the saturation dynamics is not affected by beam pre-bunching unless the initial bunching exhibits an anomalously large values.

Figure 6 does not contain further information beyond what has been discussed for U-FEL. In Sec. IV, we speculate on the possibility of exploiting the bunching induced by the CARM interaction to propose alternative operating conditions.

The mechanism determining the saturation pattern in free electron coherent sources of radiation is characterized by specific paradigmatic steps. After the linear regime, the "slowing down" of the power growth can be traced back to the interplay between the gain and the increase in power, which are responsible for

1. a loss of electron energy;
2. an increase in electron beam (e. b.) energy spread;
3. a diffusion and a rotation in the e. b. phase space, associated with the oscillation of CARM power, together with a long time damping of the oscillation amplitudes.

A synoptic view to the physics of CARM saturation is shown in Figs. 7 and 8, where we have presented the power growth vs z, characterized by an exponential increase, a slowing down, a maximum peak, and a consequent oscillation. We have chosen some points on the power curve, where we have presented the corresponding electron phase space portraits.

We have made a distinction between the growing and oscillatory parts. The first steps are characterized by a moderate perturbation of the initial phase space distribution, which increases and exhibits significant distortion for increasing z-values. At maximum power, the phase space portrait corresponds to half a rotation [Fig. 7(b)], which is completed in the successive power oscillations (Fig. 8).

The macroscopic consequences of the phase space dynamics are twofold: energy loss of the electron beam and increase in its energy spread, both shown in Fig. 9. In Fig. 9(a), we have shown the behavior of the following quantity with respect to z:

$$\epsilon(z) = 1 - \left(\frac{\gamma(z)}{\gamma_0}\right)^2, \tag{38}$$

linked to energy loss by $\gamma(z) = \sqrt{1-\epsilon(z)}\gamma_0$. It closely follows the pattern observed for power growth vs z; $\epsilon(z)$ exhibits a continuous increase till the first peak occurs, then the energy oscillates in correspondence to the spatial power oscillations (see Fig. 9).

The parameter $\epsilon(z)$ is linked to the electron beam power fractional losses, which also defines the efficiency of the device. It is measured in terms of the electron beam kinetic energy fractional losses ($\eta = (\gamma(z) - \gamma_0)/\gamma_0$), which combined with Eq. (38) yields (z^* is the position of the first peak)

$$\eta = \frac{1 - \sqrt{1-\epsilon(z^*)}}{1 - \gamma_0^{-1}}. \tag{39}$$

The same comment holds for the induced relative energy spread, presented in Fig. 9(b), which accompanies the relative energy increase in power and the phase space dynamics.

The use of the simulation parameters presented in Table I yields η around 15%, a large value compared to U-FELs (see below).

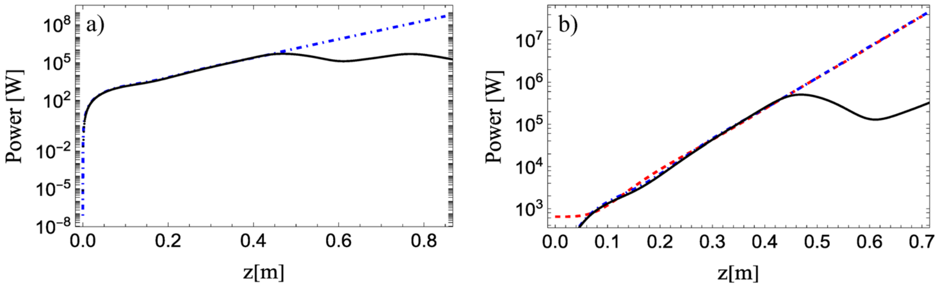

FIG. 6. (a) Power growth vs. z for a seedless process with a pre-bunched beam. Comparison between numerical simulation (continuous line) and analytical linear regime (dashed-dot line). (b) Comparison between seeded (red dot line) and seedless growth [same as (a)]. The simulation parameters used some as in Fig. 5 with the initial detuning $\Delta_0 = 6.1 \times 10^{-3}$.

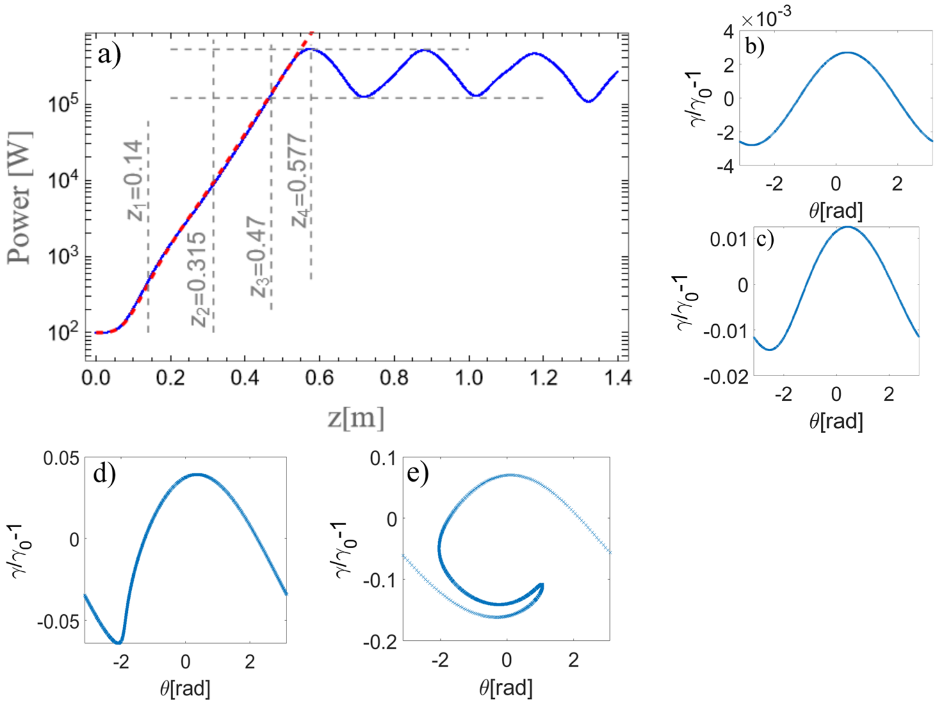

FIG. 7. (a) Power growth curve vs *z*: analytical equation (34) (dotted line) and numerical curve (solid line). Lower panels (z_a, z_b, z_c, z_d): phase space portraits at the points selected on the growth curve.

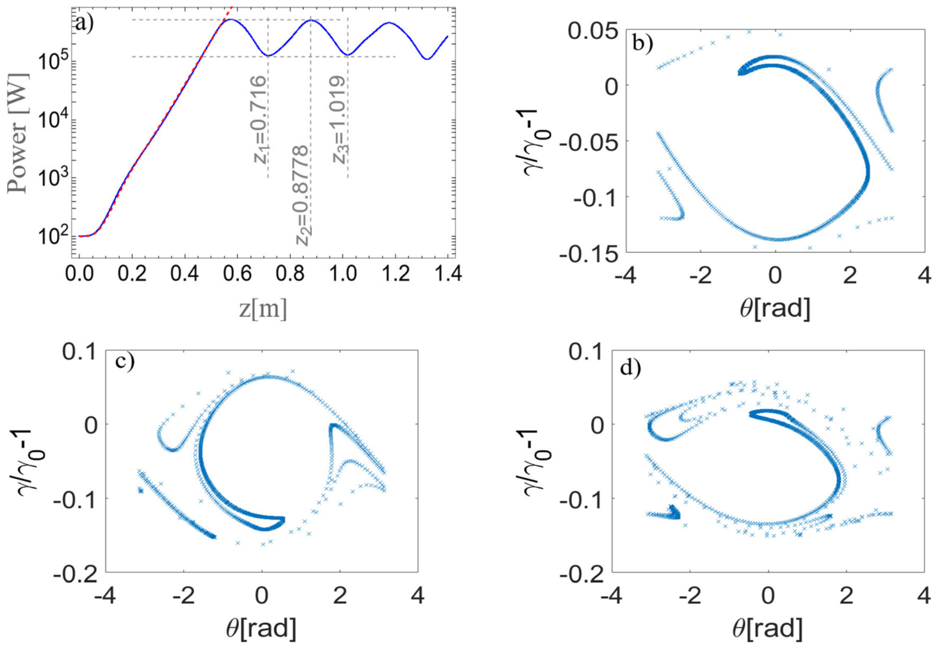

FIG. 8. Same as Fig. 7 for the post-saturated regime.

Since we are dealing with a highly nonlinear process, there is no sharp boundary between the various mechanisms and thus between causes and effects, which become increasingly entangled as *z* progresses. The macroscopic consequences of the saturation dynamics are represented by power increase, by its oscillations, and by the induced energy spread which determines (and is determined by) the phase space dynamics.

The saturation pattern is illustrated by the previous figures and the relevant physical mechanisms share a few analogies with U-FEL dynamics, as also emphasized in Ref. 34. It is however important to

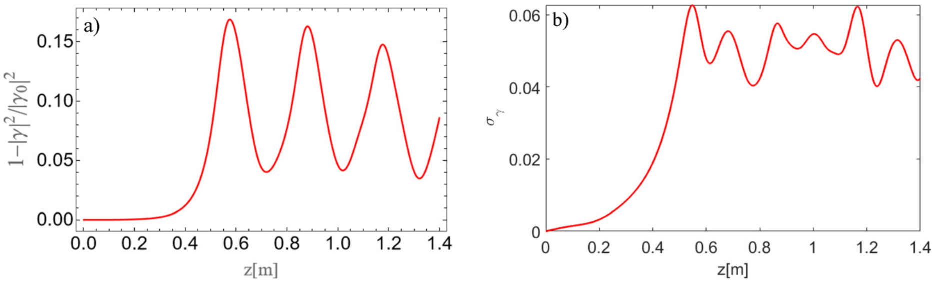

FIG. 9. (a) $1-(\gamma/\gamma_0)^2$ vs z, (b) electron beam-induced energy spread $\sigma_\gamma = \sqrt{\langle(\frac{\gamma_0-\gamma_i}{\gamma_0})^2\rangle - \langle\frac{\gamma_0-\gamma_i}{\gamma_0}\rangle^2}$ vs z.

TABLE I. Setting parameters used for the simulations.

Parameters	Values
Beam energy	0.7 MeV
Beam current	4.4 A
Pitch ($\beta_\perp/\beta_z$)	0.53
Static magnetic field (H_0)	2.93 T
β_ϕ	1.063
Resonance ω_+	140 GHz
Current density $J_{0,eff}$	0.34848×10^6
Waveguide radius	6.7 mm
Operative mode	TE_{22}

underline that the frequency selection mechanism contains important specific elements of difference, which reveal the characterizing features of the CARM devices themselves.

In Fig. 2, we have selected the CARM operating frequencies, determined by the intersection of the e-beam line with the waveguide dispersion relation. In Fig. 10, we have presented the electron line (red) and the waveguide dispersion relation (blue line), in the vicinity of the upper frequency, representing the CARM operating point (see Table I, where the parameters of the simulation have been presented).

The red line in Fig. 10 intersects the cavity dispersion curve in a point (denoted by a black dot) representing the condition of optimum gain, which realizes the transition point ($z \approx 0.14$) from the letargic region to the linear (exponential gain) regime as shown in Fig. 4. A compromise condition between the dynamically reached condition, characterizing the on set of the linear (exponential gain) regime, after the lethargic region () in the first of Fig. 7. The electron line, at the beginning of the interaction, is denoted by the magenta curve, corresponding to the chosen initial detuning. Once the interaction starts, the electrons loose energy and their representative line in Fig. 10 shifts in parallel toward lower frequencies, till a minimum value is reached when the power is at its maximum. Then, the reverse pattern is seen, where the line moves back toward higher frequencies and, on reaching a maximum value (associated with the first minimum of the power oscillations), starts oscillating in step with the power oscillations (see Fig. 11 where we have plotted the behavior of detuning vs the longitudinal coordinate z).

The physical mechanisms we have described so far are common to all free electron laser-type devices. The differences with undulator-based FEL are discussed in Sec. IV. The acronym CARM contains the term "autoresonance" and the content of Figs. 10 and 11 provides a partial justification for this terminology.

IV. CONCLUSIONS

As emphasized at the end of Sec. III, the power oscillations are characteristic features of the dynamics of free electron coherent sources. Their physical origin can be traced back to the interplay between electron energy losses and induced energy spread (see Fig. 9). Regarding the behavior of the detuning, we note that the z-position, at which the curve in Fig. 11 starts to increase significantly, corresponds

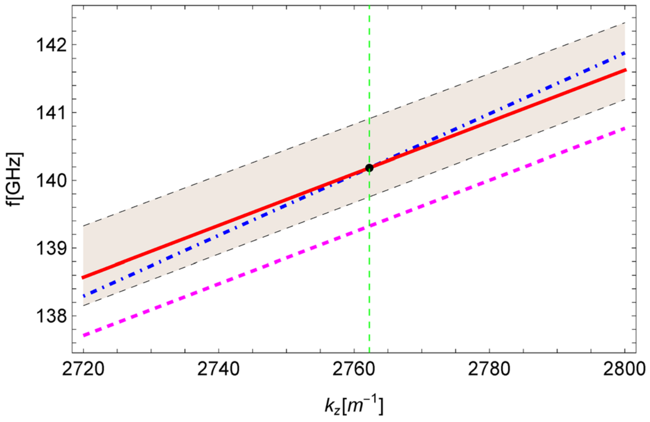

FIG. 10. Detuning and CARM frequency selection during the growth signal simulation of Fig. 7.

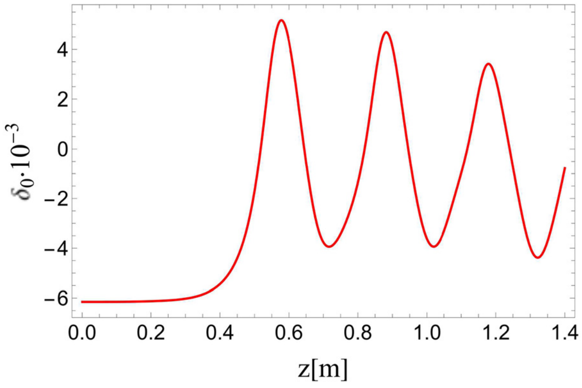

FIG. 11. Detuning shift vs z during the growth signal simulated in Fig. 7 with initial detuning $\Delta_0 = -6.1 \times 10^{-3}$.

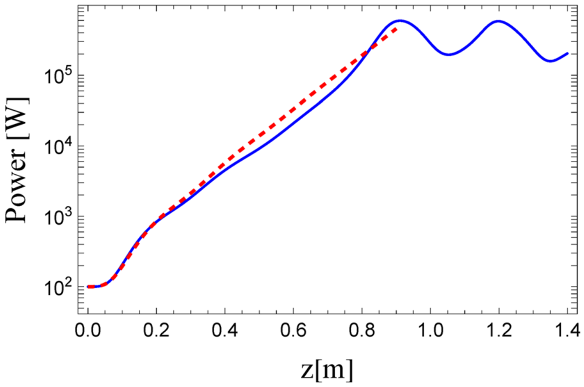

FIG. 12. Power vs z for an initial detuning of $\Delta_0 = -7.5 \times 10^{-3}$.

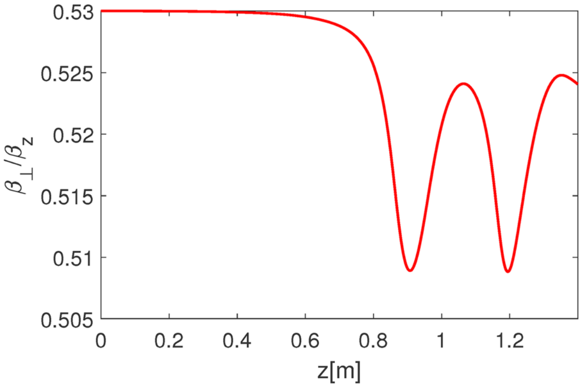

FIG. 14. Pitch $\beta_\perp/\beta_z$ vs z for the simulation presented in Fig. 7.

to a point where the power has become sufficiently large to produce a non-negligible electron energy loss. The consequent effect is therefore that the system tends to remain for a longer time in the positive gain region, thereby increasing the laser power. If we change the operating conditions, namely, we start with a larger detuning, the corresponding gain curve is the one shown in Fig. 12. The power growth is initially characterized by lower gain and the detuning remains constant for a larger z-interval (see Fig. 13). The dynamics of the growth is significantly modified, with respect to the previous case. The curve assumes a bi-logistic shape[37] and the growth rate no longer has a constant derivative. Such a behavior, due to the synchronism condition maintained for a longer time, also results in a slight increase in the final output power. This effect is well known and will not be further discussed here.[38]

We would like to emphasize that the study of FEL-like dynamics, as we have just outlined, indicates that the linear theory is not adequate to reproduce the onset of the frequency shift, as also shown by the dotted line in Fig. 12, which represents the small signal power evolution, according to the prescriptions of Sec. II.

We have already mentioned the CARM efficiency and noted (without any elaboration) that it is larger than that of the U-counterparts. The dynamics of the electrons' energy transfer along z is expressible through the parameter ϵ [see Eq. (38)], which is also used to quantify the efficiency. We have also noted that the detuning excursion is linked to the electrons' energy loss and therefore the width of this excursion is a further indirect measure of the efficiency. The maximum excursion is constrained to the width of the gain curve and the use of tapered undulators allows, e.g., to broaden this curve broadening, resulting in increased efficiency in U-FEL devices. In Fig. 14, we have presented a quantitative account of the effective field beam coupling $\beta_\perp/\beta_z$ variation vs z. The behavior of the ratio $\beta_\perp/\beta_z$ is characterized by an almost constant value till the onset of saturation. The subsequent oscillatory behavior determines the non-constancy of the CARM strength parameter and it impacts device performance, deserving an accurate discussion. The dynamics of the phase shift δ depends critically on the transverse velocity evolution and it is of paramount importance for the evolution of the CARM power.[19,39,40]

To exemplify its role, we have run the code with and without its contribution and have provided the comparison in Figs. 15 and 16, reporting the power growth curve for different values of detuning. When the shift is off, the growth exhibits an early saturation, due to an abrupt variation in detuning, which brings the system into the negative gain region. The physical origin of the phase shift is that of ensuring the self-restoring of the tuning conditions and thus the autoresonance behavior of the device.

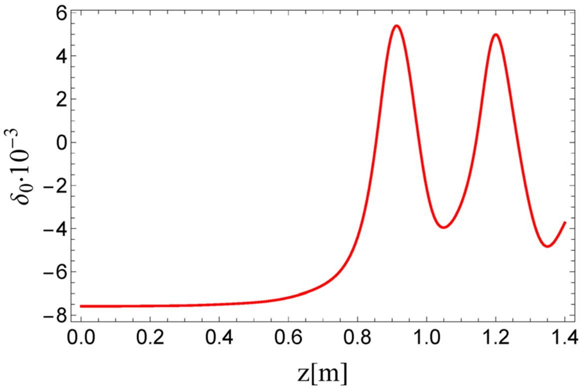

FIG. 13. Detuning shift vs z during the growth signal simulated in Fig. 12 with initial detuning $\Delta_0 = -7.5 \times 10^{-3}$.

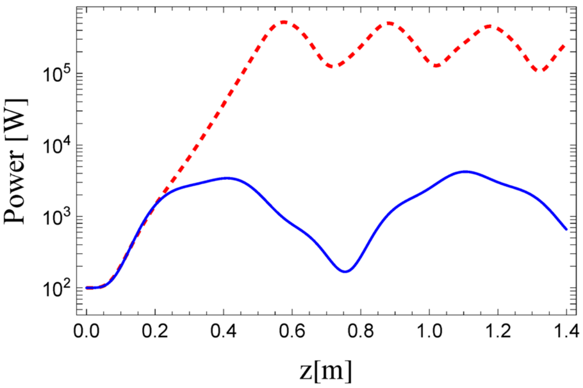

FIG. 15. Power growth vs z with (dashed line) and without (continuous line) $d\delta/dz$ term in Eq. (14).

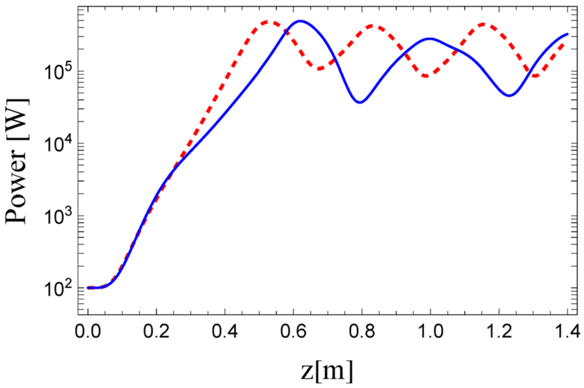

FIG. 16. Same as Fig. 15 with $\Delta_0 = 5.43 \times 10^{-3}$.

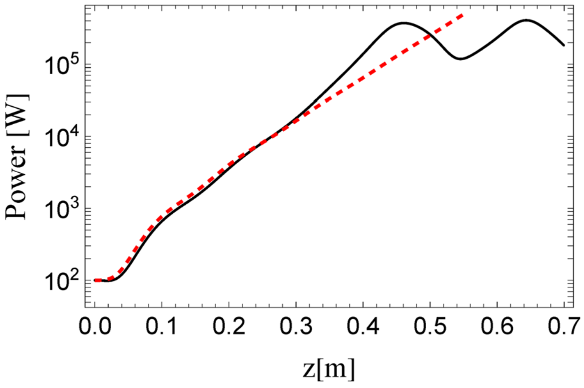

FIG. 17. Power growth linear regime comparison for $\omega_- = 2\pi \times 10^9$ with $k_z = 481.05$ and $\Delta_0 = -3.2 \times 10^{-2}$.

The last discussion has pointed out a significant difference between CARM and U-FEL devices. Another difference stems from the presence of a second resonance condition, characterizing a lower frequency mode and therefore the emergence of a CARM operation at longer wavelengths. To test this possibility, we have adjusted the simulation parameters (ω and k_z) to ensure the lasing action around the lower frequency.

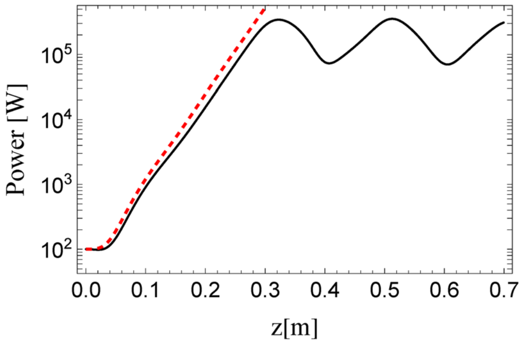

FIG. 18. Same as Fig. 17 with $\Delta_0 = -2.5 \times 10^{-2}$.

The results of our analysis are shown in Figs. 17 and 18, where we have presented the power growth curve under small and strong signal conditions. We must underline that the agreement between numerical and analytical results is qualitatively but not quantitatively satisfactory. There are different reasons for this discrepancy, including earlier manifestation of the nonlinear effects, which limits the validity of the small signal equation to a smaller z-interval.

It must be noted that Eqs. (14) and (15) hold for slowly varying amplitudes, which is insufficient for CARM operation at lower frequencies.[22] In a forthcoming investigation, we will extend the model equation without this assumption and explore CARM operation at ω_-, along with the possibility of a simultaneous lasing action at both frequencies.

The interaction-induced bunching in free electron devices is their identifying feature. Regarding undulator FELs, it is the physical mechanism allowing, not only, their existence, but the possibility of extending the associated performances (nonlinear harmonic generation,[41] segmented undulators[41]). Regarding CARM, the bunching dynamics has been the subject of accurate studies[19,40,42] and its origin (namely, whether due to inertial or force bunching) has been carefully discussed. The authors strongly recommend conducting an accurate numerical study of the relevant dynamics, along with exploring the possibility of extending the CARM operating performance.

The distinctive feature of the present analysis has been the attempt to view the CARM theory through the lens of FEL phenomenology. For this purpose, we have introduced a set of quantities [see Eqs. (3), (8), (27), and (30)–(33)] constituting the key elements of the analogy.

We emphasize that the theory we have developed is limited to 1D analysis. Its extension to three dimensions requires significant improvements, which are planned for the future, though not immediately. We are exploring the inclusion of the 3D mode structure in our analysis using a heuristic approach, which allows for the evaluation of cavity wall attenuation—previous studies have shown this effect to be modest but not entirely negligible.[46] Even though we have used data available in the literature to compare GRAAL with the three-dimensional code (CSPOT-3D) and experimental results (see Fig. 19), the comparison is satisfactory; therefore GRAAL is

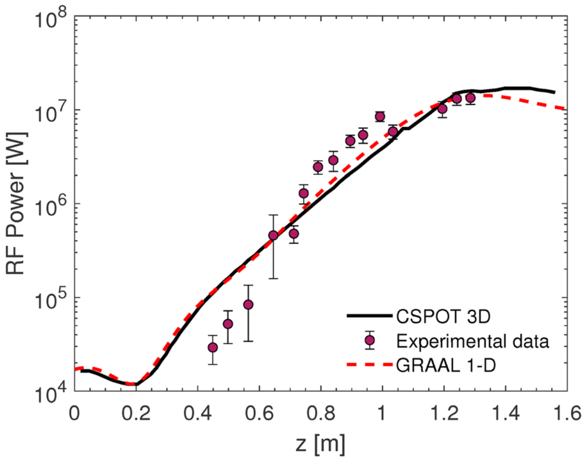

FIG. 19. CARM power growth comparison between experimental data (see Refs. 43 and 44), CSPOT-3D (see Ref. 45) as well as GRAAL 1D code.

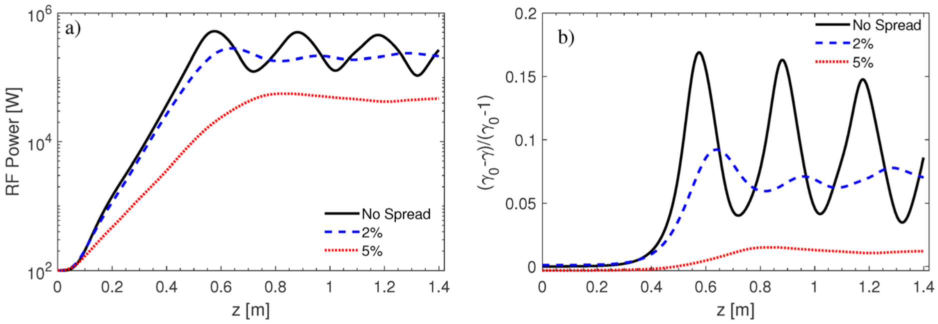

FIG. 20. (a) CARM power growth vs z without energy spread (continuous line) and with $\sigma = 2\%$ (dashed line), $\sigma = 5\%$ (dotted line). (b) Same as (a) for the efficiency $[(\gamma - \gamma_0)/(\gamma_0 - 1)]$.

considered to be suitable as a tool for the preliminary design of a CARM device.

Regarding the other approximations we note that the Small Varying Envelope Amplitude approximation is justified in Appendix A and largely applies to the parameter environment explored in this work. The beam qualities have a significant impact on the CARM performance, particularly concerning the small signal gain. Large energy spread induces an increase in the saturation length as shown in the comparison of Fig. 20. The inclusion of energy distribution in the simulation code has been performed by considering a Gaussian distribution of the energy, characterizing the distribution in terms of the rms values (σ). We have indicated how these effects occur by considering two different values of the energy spread. As expected, larger spreads produce an increase in the saturation length, a shift in the maximum power position along with its reduction. It is also evident that within a spread of 1%, no significant gain and power deterioration is observed (see also Ref. 29).

We conclude this summary by noting that we have not discussed the role of emittance, which can be fully understood only within the context of a 3D analysis. In the present 1D case, its role is viewed as an additional longitudinal contribution, quadratically added to the energy spread.

ACKNOWLEDGMENTS

The authors express their sincere appreciation to Dr. S. Sabchevski and Dr. I. Spassovsky for their assistance at every stage of this work. The careful and challenging comments of an anonymous referee and Dr. M. D. Balcazar have provided the opportunity for significant improvement in both the form and content of this article.

AUTHOR DECLARATIONS

Conflict of Interest

The authors have no conflicts to disclose.

Author Contributions

Emanuele Di Palma: Conceptualization (equal); Data curation (equal); Formal analysis (equal); Investigation (equal); Methodology (equal); Software (equal); Writing – original draft (equal). **Giuseppe Dattoli:** Conceptualization (equal); Data curation (equal); Formal analysis (equal); Investigation (equal); Methodology (equal); Software (equal); Writing – original draft (equal).

DATA AVAILABILITY

The data that support the findings of this study are available from the corresponding author upon reasonable request.

APPENDIX A: ONE-DIMENSIONAL EQUATIONS AND SIMULATION CODE DESCRIPTION

The one-dimensional CARM equations (14) and (15) are obtained by writing the Lorentz equations of a particle moving in a longitudinal static magnetic field B_0 and interacting with a co-propagating electromagnetic field,

$$\begin{aligned}\frac{d\epsilon}{dt} &= e\vec{v}_e \cdot \frac{\partial \vec{A}}{\partial t},\\ \frac{d\vec{p}}{dt} &= -e\left(-\frac{\partial \vec{A}}{\partial t} + \vec{v}_e \times \nabla \times \vec{A} + \vec{v}_e \cdot \vec{B}_0\right),\\ \epsilon &= \gamma m_e c^2,\\ \vec{p} &= \gamma m_e c\vec{\beta} = \beta_z(0,0,1) + \beta_\perp(\cos\psi,\ \sin\psi, 0),\end{aligned} \tag{A1}$$

where the vector potential $\vec{A}$ of a circularly polarized wave is governed by the following equation:

$$\begin{aligned}-\nabla^2\vec{A} + \frac{1}{c^2}\frac{\partial^2\vec{A}}{\partial t^2} &= \mu_0\vec{J},\\ \vec{A} &= \mathcal{A}_+(z)[\sin(\phi(z,t)), -\cos(\phi(z,t)), 0],\\ \phi(z,t) &= \omega t - k_{||}z + \delta(z),\end{aligned} \tag{A2}$$

where the force term $\vec{J}$ corresponds to the current generated by the charge particle flow and δ is the phase shift induced by the beam–wave interaction.

From Eqs. (A1), through a straightforward calculation, we derive Eqs. (14) for the electrons. Furthermore, using the slowly varying envelope approximation conditions, given by

$$\begin{aligned}\frac{1}{A_+}\left(\frac{dA_+}{dz}\right) &\ll k_z,\\ \frac{1}{A_+k_z}\left(\frac{d^2A_+}{d^2z}\right) &\ll k_z,\\ \frac{d\phi}{dz} &\ll k_z,\\ \frac{1}{k_z}\left(\frac{d^2\phi}{d^2z}\right) &\ll k_z,\end{aligned} \tag{A3}$$

Eq. (A2) reduces to

$$\begin{aligned} -2k_z\dot{\mathcal{A}}_+ \cdot \hat{e}_2 + 2k_z\mathcal{A}_+\dot{\delta}\cdot\hat{e}_1 &= \mu_0\vec{J}_\perp, \\ \hat{e}_1 &= (\sin(\phi), -\cos(\phi)), \\ \hat{e}_2 &= (\cos(\phi), \sin(\phi)), \\ \vec{J}_\perp &= -\frac{I_0}{\Sigma v_z}\vec{v}_\perp = -J_{0,eff}\frac{\vec{\beta}_\perp}{\beta_z}, \end{aligned} \tag{A4}$$

where Σ represents the transverse area of the operative mode in the cavity and $J_{0,eff}$ the beam density current overlapping the operative mode. Starting from Eq. (A4) and assuming $\theta = \psi - \phi + \pi/2$, through a straightforward calculation we derive Eqs. (15) for the normalized amplitude $a_+ = e\mathcal{A}_+/(mc)$ and phase δ.

The self-consistent system of differential equations used to simulate the CARM interaction couples three equations for each particle [Eqs. (14)] with the equation for amplitude and phase [Eqs. (15)] of the generated field. A numerical code implementing the fourth-order Runge–Kutta algorithm has been developed to solve the system of equations to simulate a CARM amplifier. Its main components are as follows:

- The initial setup includes the beam parameters (relativistic factor γ, beam current I_0, pitch factor $\beta_{\perp,0}/\beta_{z,0}$); the input signal [amplitude $a_+(0)$, resonance frequency ω, normalized wave phase velocity β_ϕ]; the external magnetic field $\Omega_{c,0}$ fixing the initial detuning Δ_0; the cavity parameters (cavity length L_c and the operative mode TE_{mn}, for coupling to TM_{mn} see Ref. 21); and the initial particle distribution (uniform or gaussian) in energy (γ) and phase (θ).
- The update step: For each spatial step $N_c = L_c/\Delta z$ and particle, the $3N_p + 2$ equations (with $N_p = N_\gamma N_\theta$ the number of particles) are solved using the Runge–Kutta algorithm.
- Available output data: power growth vs z—phase space $(\gamma, \dot{\gamma})$, (θ, γ), $(\theta, \dot{\theta})$ at fixed z_0—gain curve vs Δ—system efficiency vs z—induced spread vs z.

APPENDIX B: THE HIGH GAIN INTEGRAL EQUATION

In Refs. 14 and 15, we have presented the CARM constitutive equations, written in a form closely resembling the Prosnitz–Szoke–Neil formulation.[47] The standard procedure discussed, e.g., in Refs. 6 and 48 allows their reduction to a set of equations written in a pendulum-like form coupled to those of the field.

In this appendix, we summarize the (cumbersome) algebraic steps leading to an analogous reduction for the CARM case.

(a) We start from the electron-field phase angle, which can be written as

$$\frac{d\theta}{dz} = \frac{\Omega_{c0}}{\gamma c\beta_z} - \frac{k}{\beta_z}\left(1 - \frac{\beta_z}{\beta_\phi}\right) - \frac{a_+k}{\gamma\beta_\perp\beta_z}\cdot\left(1 - \frac{\beta_z}{\beta_\phi}\right)\cos(\theta) - \frac{d\delta}{dz}. \tag{B1}$$

(b) Taking an additional derivative with respect to z, we obtain

$$\begin{aligned} \frac{d^2\theta}{dz^2} = {} & \frac{a^+k}{\gamma^2\beta_\perp\beta_z}\left(1 - \frac{\beta_z}{\beta_\phi}\right)\cos(\theta)\frac{d\gamma}{dz} + \frac{a^+k}{\gamma\beta_\perp^2\beta_z}\left(1 - \frac{\beta_z}{\beta_\phi}\right)\cos(\theta)\frac{d\beta_\perp}{dz} + \frac{a^+k}{\gamma\beta_\perp\beta_z^2}\left(1 - \frac{\beta_z}{\beta_\phi}\right)\cos(\theta)\frac{d\beta_z}{dz} \\ & + \frac{a^+k}{\gamma\beta_\perp\beta_z}\frac{1}{\beta_\phi}\cos(\theta)\frac{d\beta_z}{dz} + \frac{a^+k}{\gamma\beta_\perp\beta_z}\left(1 - \frac{\beta_z}{\beta_\phi}\right)\sin(\theta)\frac{d\theta}{dz} - \frac{\omega_{c0}}{\gamma^2 c\beta_z}\frac{d\gamma}{dz} - \frac{\Omega_{c0}}{\gamma c\beta_z^2}\frac{d\beta_z}{dz} + \left[\frac{k}{\beta_z^2}\left(1 - \frac{\beta_z}{\beta_\phi}\right) + \frac{k}{\beta_z}\right]\frac{d\beta_z}{dz} - \frac{d^2\delta}{dz^2}. \end{aligned} \tag{B2}$$

(c) On replacing the derivative of the kinematic quantities with respect to z with the corresponding equation of motion implicit in Eqs. (14) and (15), neglecting the first four nonlinear terms in the field amplitude on the rhs of Eq. (B2), we eventually obtain

$$\begin{aligned} \frac{d^2\theta}{dz^2} \approx {} & \frac{a^+k}{\gamma\beta_\perp\beta_z}\left(1 - \frac{\beta_z}{\beta_\phi}\right)\sin(\theta)\left[-\frac{a^+k}{\gamma\beta_\perp\beta_z}\left(1 - \frac{\beta_z}{\beta_\phi}\right)\cos(\theta) + \frac{\omega_{c0}}{\gamma c\beta_z} - \frac{k}{\beta_z}\left(1 - \frac{\beta_z}{\beta_\phi}\right) - \frac{d\delta}{dz}\right] \\ & - \frac{\omega_{c0}}{\gamma^2 c\beta_z}\left[-a_+k\frac{\beta_\perp}{\beta_z}\sin(\theta)\right] + \left[\frac{k}{\beta_z^2}\left(1 - \frac{\beta_z}{\beta_\phi}\right) + \frac{k}{\beta_z} - \frac{\omega_{c0}}{\gamma c\beta_z^2}\right]\cdot\left[-\frac{k_z}{\beta_z\gamma}a^+\beta_\perp\sin(\theta) + a_+k\frac{\beta_\perp}{\gamma}\sin(\theta)\right] - \frac{d^2\delta}{dz^2} \\ = {} & \left\{\left(1 - \frac{\beta_z}{\beta_\phi}\right)\frac{k^2}{\gamma\beta_\perp\beta_z^2}\Delta_0 + \frac{kk_z\beta_\perp}{\gamma\beta_z^3}\Delta_0 + \frac{k^2\beta_\perp}{\beta_z^2\gamma}\left(1 - \frac{\beta_z}{\beta_\phi}\right) + \frac{k^2\beta_\perp}{\beta_z^2\gamma}\left(-\frac{k_z}{k} + \beta_z\right)\right\}a^+\sin(\theta) - \frac{d^2\delta}{dz^2} \\ = {} & H_0a^+\sin(\theta) - \frac{d^2\delta}{dz^2}, \end{aligned} \tag{B3}$$

where

$$\begin{aligned} H_0 &= \left(1-\frac{\beta_{z,0}}{\beta_\phi}\right)\frac{k^2}{\gamma_0\beta_{\perp,0}\beta_{z,0}^2}\left[\Delta_0+\beta_{\perp,0}^2+2b\Delta_0\right] \\ &\quad +\frac{k^2\beta_{\perp,0}\beta_{z,0}}{\beta_{z,0}^2\gamma}\left(-\frac{1}{\beta_\phi\beta_{z,0}}+1\right), \\ b &= \frac{\beta_{\perp,0}^2}{2\beta_\phi\beta_{z,0}(1-\beta_{z,0}/\beta_\phi)}, \\ \Delta_0 &= \frac{\Omega_{c0}}{\gamma_0\omega}-1+\frac{\beta_{z,0}}{\beta_\phi}. \end{aligned} \tag{B4}$$

The constitutive CARM equations have therefore been written in the form of a pendulum equation coupled to the field equations, as follows:

$$\begin{gathered} \frac{d^2\alpha}{d^2z}\approx H_0a_+\sin(\theta), \\ \alpha=\theta+\delta, \\ \frac{da_+}{dz}=K\left\langle\frac{\beta_\perp}{\beta_z}\sin\theta\right\rangle_{\theta_0} \quad \text{and} \quad \frac{d\delta}{dz}=-\frac{K}{a_+}\left\langle\frac{\beta_\perp}{\beta_z}\cos\theta\right\rangle_{\theta_0}. \end{gathered} \tag{B5}$$

The next step is to perform the relevant linearization. We follow a procedure analogous to that discussed in Ref. 49.

(d) The equation of motion of the complex amplitude in Eqs. (18) is written as

$$\begin{aligned} \frac{dA}{dz} &= \frac{da_+}{dz}e^{i\delta}+ia_+e^{i\delta}\frac{d\delta}{dz} \\ &= e^{i\delta(z)}\left[K\left\langle\frac{\beta_\perp}{\beta_z}\sin\theta\right\rangle_{\theta_0}-K\left\langle\frac{\beta_\perp}{\beta_z}\cos\theta\right\rangle_{\theta_0}\right] \\ &= -ie^{i\delta}K\left\langle\frac{\beta_\perp}{\beta_z}e^{i\theta}\right\rangle_{\theta_0}=-iK\left\langle\frac{\beta_\perp}{\beta_z}e^{i\alpha}\right\rangle_{\theta_0}. \end{aligned} \tag{B6}$$

(e) The pendulum equation is then cast in the following form:

$$\frac{dA}{dz}=-iK\left\langle\frac{\beta_\perp}{\beta_z}e^{i\alpha}\right\rangle_{\alpha_0}. \tag{B7}$$

The linearization procedure consists of the expansion

$$\alpha=\alpha_0+\nu_0z+\delta\alpha, \tag{B8}$$

where $\delta\alpha$ is the key quantity in the small signal approximation of the CARM equation, which allows the following expansion:

$$e^{i(\alpha_0+\nu_0z+\delta\alpha)}=e^{i(\alpha_0+\nu_0z)}e^{i\delta\alpha}=e^{i(\alpha_0+\nu_0z)}(1+i\delta\alpha). \tag{B9}$$

Thus, we eventually obtain

$$\begin{aligned} \frac{dA}{dz} &= -iK\left\langle\frac{\beta_\perp}{\beta_z}e^{i\alpha_0}\right\rangle_{\alpha_0}e^{i\nu_0z}-KH_0e^{i\nu_0z} \\ &\quad \cdot\left\langle\frac{\beta_\perp}{\beta_z}e^{i\alpha_0}\int_0^z dz'(z-z')Im\left[A(z')e^{-i(\alpha_0+\nu_0z')}\right]\right\rangle_{\alpha_0} \end{aligned} \tag{B10}$$

$$\begin{aligned} &= -iK\left\langle\frac{\beta_\perp}{\beta_z}e^{i\alpha_0}\right\rangle_{\alpha_0}e^{i\nu_0z}+iKH_0e^{i\nu_0z}\left\langle\frac{\beta_\perp}{\beta_z}e^{i\alpha_0}\right. \\ &\quad \left.\times\int_0^z dz'(z-z')\frac{A(z')e^{-i(\alpha_0+\nu_0z')}-A^*(z')e^{i(\alpha_0+\nu_0z')}}{2}\right\rangle_{\alpha_0} \end{aligned} \tag{B11}$$

$$\begin{aligned} &= -iK\left\langle\frac{\beta_\perp}{\beta_z}e^{i\alpha_0}\right\rangle_{\alpha_0}e^{i\nu_0z}+\frac{i}{2}KH_0\left\langle\frac{\beta_\perp}{\beta_z}\right\rangle_{\alpha_0} \\ &\quad \times\int_0^z dz'(z-z')A(z')e^{i\nu_0(z-z')}-\frac{1}{2}KH_0\left\langle\frac{\beta_\perp}{\beta_z}e^{2i\alpha_0}\right\rangle_{\alpha_0} \\ &\quad \times\int_0^z dz'(z-z')A^*(z')e^{i\nu_0(z+z')}. \end{aligned} \tag{B12}$$

Assuming that the bunching weak enough that bunching at higher harmonics can be neglected, we end up with

$$\begin{aligned} \frac{dA}{dz} &= -iK\left\langle\frac{\beta_\perp}{\beta_z}e^{i\alpha_0}\right\rangle_{\alpha_0}e^{i\nu_0z}+\frac{i}{2}KH_0\left\langle\frac{\beta_\perp}{\beta_z}\right\rangle_{\alpha_0} \\ &\quad \cdot\int_0^z dz'(z-z')A(z')e^{i\nu_0(z-z')}. \end{aligned} \tag{B13}$$

If we neglect the first term in Eq. (B13), it reduces to

$$e^{-i\nu_0z}D_zA=\frac{i}{2}KH_0b_2D_z^{-2}\left(A(z)e^{-i\nu_0(z)}\right), \tag{B14}$$

where the symbol with negative derivative denotes the Cauchy repeated integral given by

$$D_z^{-n}f(z)=\frac{1}{(n-1)!}\int_0^z(z-z')^{n-1}f(z')dz'. \tag{B15}$$

Keeping successive derivatives with respect to z on both sides of Eq. (B14), we obtain the third-order differential equation presented in Eq. (29).

The relevant solution is obtained by solving the cubic equation associated with the characteristic polynomial, which is achieved using the Cardano rule,

$$\begin{aligned} A(z,\nu_0) &= \frac{A(0)}{3(p+q-\nu_0)}e^{\frac{2i}{3}\nu_0z} \\ &\quad \times\left\{(p+q+\nu_0)e^{\frac{i}{3}(p+q)z}+2(p+q-2\nu_0)e^{\frac{i}{6}(p+q)z}\right. \\ &\quad \left.\times\left[\cosh\left(\frac{\sqrt{3}}{6}(p-q)z\right)+i\frac{\sqrt{3}\nu_0}{q-p}\sinh\left(\frac{\sqrt{3}}{6}(p-q)z\right)\right]\right\}, \\ p &= \left[\frac{1}{2}(r+\sqrt{d})\right]^{1/3}, \quad p=\left[\frac{1}{2}(r-\sqrt{d})\right]^{1/3}, \\ r &= 27KH_0b_2+2\nu_0^3, \quad d=27KH_0b_2(27KH_0b_2+4\nu_0^3). \end{aligned} \tag{B16}$$

Interaction-induced bunching is the primary mechanism enabling nonlinear harmonic generation.[50,51] This effect has been exploited in U-FEL devices to enhance their tunability, see, e.g., Refs. 41 and 52 and references therein. We will discuss, in a separate research study, the possibility of exploiting an analogous mechanism in CARM devices to improve their performance.

APPENDIX C: GRAAL CODE STABILITY BENCHMARKS AND OUTPUT EFFICIENCY SENSITIVITY

The numerical code is based on a macro-particle description and a fourth-order Runge–Kutta method. An crucial aspect is

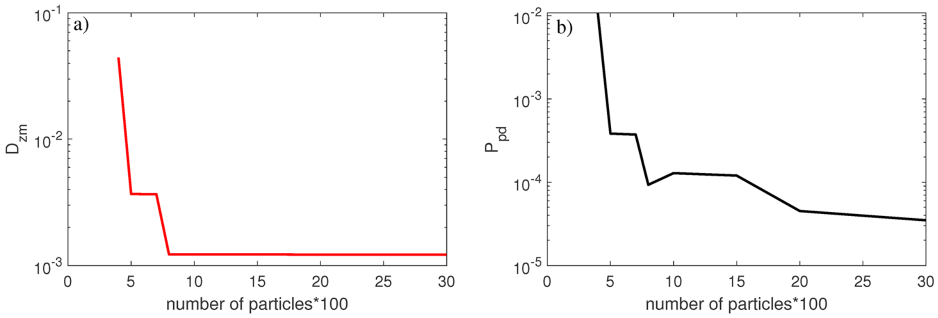

FIG. 21. Code stability convergence check vs the number of macro-particles. (a) Fractional peak position and (b) fractional maximum power.

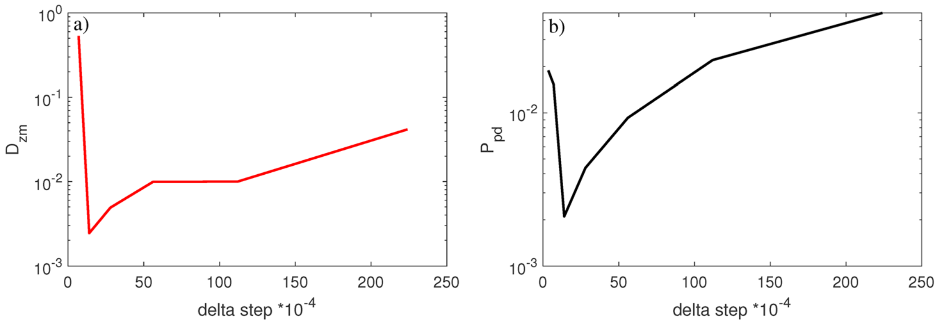

FIG. 22. Same as Fig. 21 vs the step size.

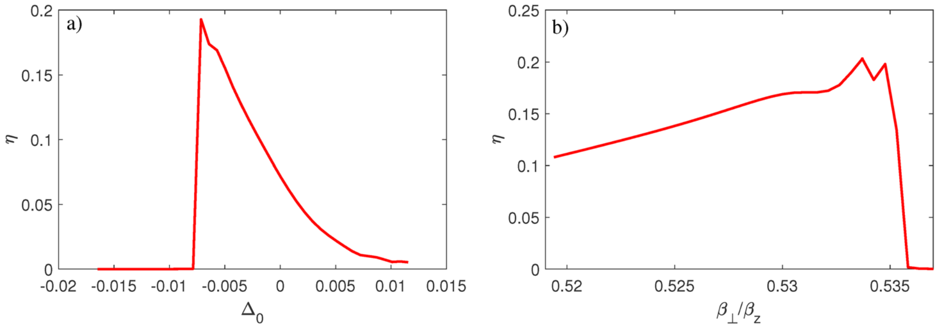

FIG. 23. (a) Efficiency vs Δ_0. (b) Efficiency vs $\beta_\perp/\beta_z$.

benchmarking its convergence with respect to the number of macro-particles and the Runge–Kutta step size. Due to the complexity of the code, parameters must be defined to characterize the reliability of the results; we have chosen the value of the first peak power (*Pp*) and its position along the z-axis (*zm*).

In Figs. 21 and 22, we have presented the quantities

$$D_{zm} = \frac{zm(i) - zm(i-1)}{zm(i)},\qquad P_{pd} = \frac{Pp(i) - Pp(i-1)}{Pp(i)}, \tag{C1}$$

where i is the number of particle (nr.)/size step (ss.) counter. Regarding convergence to stability vs nr., there is a clear indication that the threshold can be fixed to ~ 2000 (see Fig. 21). Concerning the step size, the optimum is obtained for ss. $\sim 1.7 \times 10^{-3}$ (see Fig. 22). The optimal step size results primarily from the decrease in the Runge–Kutta error with the decrease in step size and increase in the round-off error with decrease in the step size. Additionally, very small step sizes can lead to issues with non-conservation of energy.

From a practical standpoint, it is important to assess the sensitivity of the efficiency to variations in the design parameters. In Figs. 23(a) and 23(b), the efficiency is shown as a function of the detuning and pitch parameter, respectively.

REFERENCES

[1] J. Pierce, "Theory of the beam type as amplifier at microwaves," Proc. IRE **35**, 111–124 (1947).

[2] R. Q. Twiss, "Radiation transfer and the possibility of negative absorption in radio astronomy," Aust. J. Phys. **11**, 564–579 (1958).

[3] J. Schneider, "Stimulated emission of radiation by relativistic electrons in a magnetic field," Phys. Rev. Lett. **2**, 504 (1959).

[4] A. V. Gaponov, M. I. Petelin, and V. Yulpatov, "The induced radiation of excited classical oscillators and its use in high-frequency electronics," Radiophys. Quantum Electron. **10**, 794–813 (1971).

[5] M. Petelin, "On the theory of ultrarelativistic cyclotron self-resonance masers," Radiophys. Quantum Electron. **17**, 686–690 (1974).

[6] A. Renieri, W. B. Colson, and C. Pellegrini, *Laser Handbook, Vol. 6* (North-Holland Pub. Co., 1990).

[7] D. Varian, *The Inventor and the Pilot: Russell and Sigurd Varian* (Pacific Books, 1983), p. 187.

[8] A. S. Gilmour, Jr., *Klystrons, Traveling Wave Tubes, Magnetrons, Crossed-Field Amplifiers, and Gyrotrons* (Artech House, 2011).

[9] R. Smith-Rose, "The invention of the traveling-wave tube," Electron. Power **11**, 36 (1965).

[10] S. E. Tsimring, *Electron Beams and Microwave Vacuum Electronics* (John Wiley & Sons, 2006).

[11] V. Flyagin, A. Gaponov, I. Petelin, and V. Yulpatov, "The gyrotron," IEEE Trans. Microwave Theory Tech. **25**, 514–521 (1977).

[12] N. S. Ginzburg, G. Nusinovich, and N. Zavolsky, "Theory of non-stationary processes in gyrotrons with low q resonators," Int. J. Electron. Theor. Exp. **61**, 881–894 (1986).

[13] G. S. Nusinovich, *Introduction to the Physics of Gyrotrons* (JHU Press, 2004).

[14] S. Sabchevski, M. Y. Glyavin, and G. Nusinovich, "The progress in the studies of mode interaction in gyrotrons," J. Infrared, Millimeter, Terahertz Waves **43**, 1–47 (2022).

[15] S. Sabchevski, "Fundamentals of electron cyclotron resonance and cyclotron autoresonance in gyro-devices: A comprehensive review of theory," Appl. Sci. **14**, 3443 (2024).

[16] M. Thumm, "State-of-the-art of high-power gyro-devices: 2025 update of experimental results," J. Infrared, Millimeter, Terahertz, Waves **46**, 1–154 (2025).

[17] G. Dattoli, E. Di Palma, S. Pagnutti, and E. Sabia, "Free electron coherent sources: From microwave to x-rays," Phys. Rep. **739**, 1–51 (2018).

[18] A. Curcio, G. Dattoli, and E. D. Palma, *Backscattering Sources, Volume 1: Theoretical Framework and Thomson Backscattering Sources* (IOP Publishing, 2024).

[19] V. L. Bratman, N. Ginzburg, G. Nusinovich, M. Petelin, and P. Strklkov, "Relativistic gyrotrons and cyclotron autoresonance masers," Int. J. Electron. Theor. Exp. **51**, 541–567 (1981).

[20] C. Chen and J. S. Wurtele, "Linear and nonlinear theory of cyclotron autoresonance masers with multiple waveguide modes," Phys. Fluids B **3**, 2133–2148 (1991).

[21] H.-Y. Yao, C.-C. Chen, and T.-H. Chang, "Starting behaviors of the TM-mode gyrotrons," Phys. Plasmas **27**, 022113 (2020).

[22] A. W. Fliflet, "Linear and non-linear theory of the doppler-shifted cyclotron resonance maser based on te and tm waveguide modes," Int. J. Electron. Theor. Exp. **61**, 1049–1080 (1986).

[23] V. L. Bratman, G. Denisov, B. Kol'Chugin, S. Samsonov, and A. Volkov, "Experimental demonstration of high-efficiency cyclotron-autoresonance-maser operation," Phys. Rev. Lett. **75**, 3102 (1995).

[24] B. Danly, J. Davies, K. Pendergast, R. Temkin, and J. Wurtele, "High-frequency cyclotron autoresonance maser amplifier experiments at MIT," Proc. SPIE **1061**, 243–247 (1989).

[25] M. Caplan, B. Kulke, D. Bubp, D. McDermott, and N. Luhmann, "A 250 GHz CARM oscillator experiment driven by an induction Linac," Nucl. Instrum. Methods Phys. Res., Sect. A **304**, 200–203 (1991).

[26] R. B. McCowan, A. W. Fliflet, S. H. Gold, W. Black, A. Kinkead, V. L. Granatstein, and M. S. Sucy, "The design of a 100-GHz CARM oscillator experiment," IEEE Trans. Electron Devices **36**, 1968–1975 (1989).

[27] N. Ginzburg, V. Y. Zaslavsky, A. Malkin, N. Y. Peskov, and A. Sergeev, "Application of modified Bragg structures in high-power submillimeter cyclotron autoresonance masers," Radiophys. Quantum Electron. **59**, 1017–1025 (2017).

[28] K. Pendergast, B. Danley, R. Temkin, and J. Wurtele, "Self-consistent simulation of cyclotron autoresonance maser amplifiers," IEEE Trans. Plasma Sci. **16**, 122–128 (1988).

[29] See https://www.fel.enea.it/booklet-presentation.html for G. Dattoli, P. Ottaviani, and S. Pagnutti, "Booklet of FEL design" (2007).

[30] F. Ciocci, G. Dattoli, A. Torre, and A. Renieri, "Free electron lasers as insertion devices," in *Insertion Devices for Synchrotron Radiation and Free Electron Laser* (World Scientific, 2000), pp. 237–286.

[31] G. Nusinovich, P. Latham, and H. Li, "Efficiency of frequency up-shifted gyrodevices: Cyclotron harmonics versus CARM's," IEEE Trans. Plasma Sci. **22**, 796–803 (1994).

[32] J. R. Pierce, "Traveling-wave tubes," Bell Syst. Techn. J. **29**, 189–250 (1950).

[33] P. Wong, P. Zhang, and J. Luginsland, "Recent theory of traveling-wave tubes: A tutorial-review," Plasma Res. Express **2**, 023001 (2020).

[34] G. Dattoli, E. Di Palma, S. Licciardi, and E. Sabia, "Free electron laser high gain equation and harmonic generation," Appl. Sci. **11**, 85 (2020).

[35] G. Dattoli, S. Pagnutti, P. Ottaviani, and V. Asgekar, "Free electron laser oscillators with tapered undulators: Inclusion of harmonic generation and pulse propagation," Phys. Rev. Spec. Top. Accel. Beams **15**, 030708 (2012).

[36] C. S. Withers and S. Nadarajah, "Power series solutions to volterra integral equations," Appl. Math. Comput. **218**, 2353–2363 (2011).

[37] Z. Dong, Y. Yang, W. Cai, Y. He, M. Chai, B. Liu, X. Yu, S. W. Banks, X. Zhang, A. V. Bridgwater *et al.*, "Theoretical analysis of double logistic distributed activation energy model for thermal decomposition kinetics of solid fuels," Ind. Eng. Chem. Res. **57**, 7817–7825 (2018).

[38] X. Wang, T. Watanabe, Y. Shen, R. Li, J. Murphy, T. Tsang, and H. Freund, "Efficiency enhancement using electron energy detuning in a laser seeded free electron laser amplifier," Appl. Phys. Lett. **91**, 181115 (2007).

[39] V. Bratman, G. Denisov, N. Ginzburg, and M. Petelin, "FEL's with Bragg reflection resonators: Cyclotron autoresonance masers versus ubitrons," IEEE J. Quantum Electron. **19**, 282–296 (1983).

[40] T. Kho and A. Lin, "Efficiency dependence on beam current and input power in a cyclotron autoresonance maser amplifier," Phys. Fluids B **2**, 822–827 (1990).

[41] H. Freund, S. Biedron, and S. Milton, "Nonlinear harmonic generation in free-electron lasers," IEEE J. Quantum Electron. **36**, 275–281 (2000).

[42] A. Gaponov, "Instability of a system of excited oscillators with respect to electromagnetic perturbations," Sov. Phys. JETP **12**, 232–298 (1960).

[43] G. Bekefi, A. DiRienzo, C. Leibovitch, and B. G. Danly, "35 GHz cyclotron autoresonance maser amplifier," Appl. Phys. Lett. **54**, 1302–1304 (1989).

[44] A. C. DiRienzo, G. Bekefi, C. Chen, and J. S. Wurtele, "Experimental and theoretical studies of a 35 GHz cyclotron autoresonance maser amplifier," Phys. Fluids B **3**, 1755–1765 (1991).

[45] C. Chen, B. G. Danly, J. A. Davies, W. L. Menninger, J. S. Wurtele, and G. Zhang, "CARM amplifier theory and simulation," Nuclear Instrum. Methods Phys. Res. Sec. A **304**, 593–600 (1991).

[46] S. Ceccuzzi, "Modal techniques for microwave components in fusion engineering and for periodic structures applied to directive antennas," Ph.D. thesis (Roma Tre University of Rome Italy, 1995).

[47] D. Prosnitz, A. Szoke, and V. Neil, "High-gain, free-electron laser amplifiers: Design considerations and simulation," Phys. Rev. A **24**, 1436 (1981).

[48] G. Dattoli, A. Galli, and P. L. Ottaviani, "One-dimensional simulation of FEL including high gain regime, saturation prebunching and harmonic generation," Technical Report No. RT/INN/93/09 (C.R. Enea Frascati, 1993).

[49] G. Dattoli and P. L. Ottaviani, "FEL small signal dynamics and electron beam prebunching," Technical Report No. RT/INN/93/10 (C.R. Enea Frascati, 1993).

[50] Y. K. Kalynov, A. V. Savilov, and E. S. Semenov, "Parasitic excitation of fundamental-cyclotron-harmonic waves in high-harmonic gyrotrons," Phys. Plasmas **28**, 113105 (2021).

[51] Y. M. Guznov, A. N. Leontyev, R. M. Rozental, A. S. Sergeev, I. V. Zotova, and N. S. Ginzburg, "Tunable multi-frequency radiation source based on gyrotron with pre-modulated beam," IEEE Electron Device Lett. **43**, 809–812 (2022).

[52] W. Colson, "The nonlinear wave equation for higher harmonics in free-electron lasers," IEEE J. Quantum Electron. **17**, 1417–1427 (1981).